Novel Refractory High-Entropy Metal-Ceramic Composites with Superior Mechanical Properties

Xin Chen[1,#], Fei Wang[1,#], Xiang Zhang[1], Shanshan Hu[2], Xingbo Liu[2], Samuel Humphry-Baker[3], Michael Gao[4], Lingfeng He[5], Yongfeng Lu[6], Bai Cui[1,*]

[1] Department of Mechanical & Materials Engineering, University of Nebraska–Lincoln, Lincoln, NE 68588, USA

[2] Department of Mechanical and Aerospace Engineering, West Virginia University, Morgantown, WV 26506, USA

[3] Department of Materials, Imperial College London, South Kensington Campus, London SW7 2AZ, UK

[4] National Energy Technology Laboratory, 1450 Queen Ave SW, Albany, OR 97321.

[5] Idaho National Laboratory, Idaho Falls, ID 83415, USA

[6] Department of Electrical & Computer Engineering, University of Nebraska-Lincoln, Lincoln, NE 68588, USA

*Corresponding author. Tel.: +1 (402) 472-5740; fax: +1 (402) 472-1465; email: bcui3@unl.edu.

[#]These authors contributed equally to this work.

Abstract

A new concept of refractory high-entropy metal-ceramic composites (HEMCC) has been proposed that combines the outstanding physical properties of both high-entropy alloy (HEA) and high-entropy ceramic (HEC). As the first HEMCC system, to the best of our knowledge, TiTaNbZr-(TiTaNbZr)C, has been developed by a powder metallurgy process. The HEA and HEC phases exhibit body-centered cubic (BCC) and rock-salt B1 crystal structures, respectively, and both phases have non-equimolar chemical compositions. With the increase of the HEC phase in HEMCC, the hardness is enhanced while the density and fracture toughness are decreased. HEA50C sintered from 50 vol.% HEA and 50 vol.% HEC precursor powders shows a favorable combination of flexural strength (541±48 MPa) and fracture toughness (6.93±0.27 $MPa \cdot m^{1/2}$) at room temperature and a high compressive strength at 1300 ºC (275 MPa). The optimized mechanical performance of HEMCC might be attributed to the combination of the ductile HEA and strong HEC phases, smaller grain size, and crack arrest at HEC/HEA interfaces.

Keywords: high-entropy alloy (HEA); high-entropy ceramic (HEC); mechanical property

1. Introduction

Advanced materials with outstanding phase stability, high-temperature mechanical strength, corrosion and irradiation resistance in extreme environments are critical for multiple applications such as gas turbine engine blades, gas-cooled fast reactors, tokomak fusion systems, and hypersonic vehicles. Currently, Ni- or Co-based superalloys [1], W- or Nb-based refractory alloys [2], and SiC_f/SiC composites [3] are the main candidates for applications with a service temperature over 1000 ºC. However, these materials fall short in meeting one or more of the required properties in extreme environments. For example, the operating temperatures of Ni- or Co-based superalloys are bottlenecked by their relatively low melting points (i.e., T_m of Ni=1455 ºC, T_m of Co=1495ºC) [4]. Refractory alloys such as C-103 (Nb-10%Hf-1%Ti) and TZM (Mo-0.5%Ti-0.8% Zr-0.02%C) [5] are characterized by high bulk density, low oxidation resistance [6,7], and irradiation embrittlement at temperatures below 30% of their melting points [8]. Ceramic materials generally have higher melting temperatures and high-temperature strength than those of metal alloys, but their applications are hindered by their intrinsic brittleness and low fracture toughness.

In recent years, the novel concept of “multi-principal component” has opened up new possibilities for discovering and developing novel materials with more complex compositions

and superior properties by exploring the center region of the phase diagrams [9,10]. These "high entropy" materials including high-entropy alloys (HEAs) and high-entropy ceramics (HECs) have become a hot topic of the research field. HEAs, such as NiCoFeMnCr [11] or NbMoTaW [12], contain four or more metallic elements in equimolar or near-equimolar concentrations that form a single-phase lattice structure. HECs, such as $(Hf_{0.2}Zr_{0.2}Ta_{0.2}Nb_{0.2}Ti_{0.2})C$ [13,14] or $(Hf_{0.2}Zr_{0.2}Ta_{0.2}Mo_{0.2}Ti_{0.2})B_2$ [15], are ceramic materials in which multiple metal elements in equal or near-equal atomic ratios in the metal positions while a nonmetal element (e.g., C, B, O) occupies the anion position. These "high entropy" materials have a broad composition space in a single-phase solid solution, which can be used to tailor physical and chemical properties to meet the complicated requirements for the specific applications. Although this manuscript adopts the common terminology of "high entropy" materials, this group of materials may be better referred to as "multi-principal component" materials to avoid confusions. Recent studies indicate that the thermodynamic stability of high-entropy carbides may not be controlled by entropy stabilization but through the competition between entropy and enthalpy of mixing [16,17]. In addition, the concept of compositionally complex alloys [18] and ceramics [19] have also been proposed to include single-phase non-equimolar compositions.

Refractory HEAs with a body-centered cubic (BCC) structure have been reported to exhibit higher thermal stability and high-temperature strength than the traditional Ni-based superalloys, especially at temperatures above 1000 ºC [20,21]. Senkov et al. [22] reported that both NbMoTaW and VNbMoTaW HEAs have yield strengths of 840 and 550 MPa, respectively, at 1000 ºC, which are much higher than those of nickel superalloys Inconel 718 and Haynes 230 (~180 MPa). On the other hand, hardness of high-entropy carbides is much higher than the estimated value by the rule-of-mixture of constitute monocarbides, which may be related to the mechanisms of mass inhomogeneity and solid solution hardening. Compared to individual monocarbides, a number of high entropy carbides can retain their flexural strength to higher temperatures [9]. Feng et al. [23] reported that the flexural strength of $Hf_{0.2}Zr_{0.2}Ta_{0.2}Nb_{0.2}Ti_{0.2})C$ is above 400 MPa from room temperature to 1800 ºC, while those of monocarbides such as TiC, TaC and HfC are decreased to be less than 400 MPa at 1400 ºC.

Metal-ceramic composites may combine the microstructures and physical properties of both metals and ceramic materials to achieve an attractive combination of hardness, strength, and toughness. Previous studies reported either HEA or HEC as the matrix phase, with the addition of ceramic or metal particles with a simple composition (not a "high entropy" phase) as the strengthening phases. For example, Wei et al. [24] fabricated $MoNbRe_{0.5}W$-$(TaC)_x$ composites by vacuum arc melting, which formed an eutectic microstructure consisting of alternate layers of BCC and MC phases (M=metal). Microhardness, yield

strength and compressive strength of these composites are improved significantly with the addition of TaC. Zhou et al. [25] developed WC-AlCrFeCoNi-cemented carbide composites by mechanical milling and sintering at 1300 to 1450 °C, which exhibited a high compressive strength up to 4395 MPa due to the inhibition of grain growth of WC by the HEA phase (10 or 20 mass%). Zhang et al. [26] used CrMnFeCoNi HEA as a sintering aid of B_4C ceramics during spark plasma sintering at 1500 to 2100 °C. The rupture strength of B_4C-5 vol.% HEA composite (619 MPa) was 37% higher than that of B_4C ceramics. Recently, Arai et al. [27] fabricated $TiZrHfNbTaB_x$ using arc melting, which vary from HEA (when x=0, 0.1, 1) to HEC (when x=10) depending on the boron content. $TiZrHfNbTaB_x$ (x = 0.1 or 1) showed a BCC matrix with MB (M = Ti, Zr, Hf, Nb, Ta) phases, while $(TiZrHfNbTa)B_2$ (when x=10) exhibited MB_2 structure. The Vickers hardness and Young's modulus of $TiZrHfNbTaB_x$ increased with an increasing B-content due to the formation of borides.

This study aimed to explore a new concept of refractory high-entropy metal-ceramic composites (HEMCC) for applications in extreme environments [28]. HEMCC is a unique material that contains both HEA and HEC phases in its microstructure. Compared to the existing HEAs or HECs, the novelty of HEMCC is that the second phase is also high-entropy. This paper presents the synthesis, microstructure, and mechanical properties of the first HEMCC system, TiTaNbZr-(TiTaNbZr)C.

2. Experimental process

TiTaNbZr-(TiTaNbZr)C HEMCC were synthesized by spark plasma sintering (SPS) process. Commercially available TiC, TaC, NbC, ZrC, Ti, Ta, Nb, and Zr (99.5%, powder size < 45 μm) powders from Alfa Aesar were used as starting materials. The metal element powders of Ti, Ta, Nb, and Zr were mixed in an equimolar composition (Ti: Ta: Nb: Zr =1: 1: 1: 1) and ball milled at 400 rpm for 30 h to form HEA precursor powders. The ceramic powders of TiC, TaC, NbC, and ZrC were mixed in an equimolar composition (TiC: TaC: NbC: ZrC =1: 1: 1: 1) and ball milled at 250 rpm for 6 h to form HEC precursor powders. HEA and HEC precursor powders were then mixed in specific volume ratios (0, 25, 50, 75, and 100% volume percentage of HEC) and ball milled at 250 rpm for 8 h. All the ball milling processes were performed by a planetary ball mill (Model Pulverisette 7, Fritsch Gmbh) using stainless steel balls of 10 mm in diameter with a ball-to-powder ratio of 5:1, which was located inside a glove box filled with Ar gas to avoid oxidation of metal and carbide powders.

Sintering of the ball-milled powders (0, 25, 50, and 75 vol.% HEC) was conducted on a SPS system (Model 10-4, Thermal Technologies) under a vacuum level of 2×10^{-2} Torr. The sintering conditions of the HEMCC and HEA were 1500 ℃ for 10 min at a pressure of 50 MPa. However, since HEC samples sintered at 1500 ℃ are porous and the HEC phase was

not formed, their sintering temperature condition was increased to 2000 ℃ for 10 min at a pressure of 50 MPa, following our previous work [29]. The heating and cooling rates for all these SPS processes were 100 ℃/min. The as-synthesized samples were discs with a diameter of 20 mm and a thickness of 3~5 mm, which were mechanically polished to remove the surface contamination by graphite molds. Subsequently, they were polished using diamond lapping films with a surface roughness of 15, 9, 6, 3, and 1 μm to achieve a mirror finish. The SPSed HEMCC samples were labeled as follows: HEA0C (sintered from 100 vol.% HEA precursor powders), HEA25C (sintered from 75 vol.% HEA+25 vol.% HEC precursor powders), HEA50C (sintered from 50 vol.% HEA+50 vol.% HEC precursor powders), HEA75C (sintered from 25 vol.% HEA+75 vol.% HEC precursor powders), and HEA100C (sintered from 100 vol.% HEC precursor powders).

Sample Phases were identified by X-ray diffraction on a diffractometer (AXS D8 Discover, Bruker) operated at 40 kV and 44 mA with the Cu K_α radiation. Scanning electron microscopy (SEM) of microstructures was conducted on a focused ion beam (FIB)/SEM dual-beam workstation (Helios 660 NanoLab, FEI) using the secondary electron imaging mode. Energy-dispersive X-ray spectroscopy (EDS) was performed by an EDS detector (Octane Super, EDAX) to reveal the element distribution. To assess the presence of steel contamination during planetary ball milling, EDS point analysis was conducted to reveal elemental composition information for the milled powder. The theoretical density of each sample was calculated using the rule of mixtures from the volume fractions of HEA and HEC phases. The real density of the samples was measured by the Archimedes method. The porosity of the samples was measured from SEM images. The grain size was estimated from the SEM images of the polished surface and fracture morphology. Scanning transmission electron microscopy (STEM) with EDS characterizations was carried out on a Thermo Scientific Talos F200X field emission gun (FEG) scanning/transmission electron microscope (S/TEM) equipped with ChemiSTEM^{TM} and operated at 200 kV. STEM-EDS was used for elemental mapping and composition analysis. All EDS quantifications were in the Thermo Scientific Velox^{TM} software using the default Brown-Powell ionization cross-section and multi-polynomial models for background correction. Selected-area electron diffraction patterns and STEM-EDS results were combined for phase identification. TEM foils were extracted and ion-milled to electron transparency by Ga^+ ions in the FIB/SEM dual-beam workstation.

Vickers hardness was measured on a hardness tester (Tukon 2500, Wilson) with 9.8 N load and 15 s dwell time. The nanohardness was measured by nanoindentations on a triboindentor (Hysitron TI 950, Bruker) with a pyramid diamond Berkovich tip at 8000 μN load and 5 s dwell time. The grid nanoindentation technique was used to map the nanomechanical properties including elastic modulus and nanohardness [30]. The rectangular grid mapping

mode was used to obtain their spatial maps. The grid spacing in both the vertical and horizontal directions was set at 5 μm, which is more than 20 times the indentation depth of a Berkovich tip on our samples to prevent geometric overlap of indents and mitigate any influence from the residual strain field of neighboring indents [31]. Flexural strength was measured by the three-point bending test using rectangular bars of 18×2×3 mm^3 without a notch (MTS 810 materials testing system). The standard equation for the flexural strength in three-point flexure is as follows:

$$S = \frac{3PL}{2bd^2} \quad (1)$$

Where P is the break force, L is the support span, b is the specimen width, and d is the specimen thickness.

Fracture toughness was measured by the single-edge notched beam (SENB) method using rectangular bars (18×3×4 mm^3) with a notch of 1 mm depth and a 0.3 mm width in the center. The specimen size was scaled down due to limitations from the graphite mold dimensions in the SPS system. However, the ratio of dimensions in these sub-size specimens was maintained the same as the standard full-size specimens in the ASTM C1421 standards of SENB tests to ensure the representative mechanical behavior. The span size of both flexural strength and fracture toughness test specimens was 15 mm, and the crosshead speed was 0.2 mm/min. The fracture toughness was calculated based on the equation [32]:

$$\mathrm{K}_{IC} = \frac{3P(S/W)\alpha^{1/2}(1.99-\alpha(1-\alpha)(2.15-3.93\alpha+2.7\alpha^2))}{2BW^{1/2}(1+2\alpha)(1-\alpha)^{3/2}}, \quad (2)$$

where $\alpha = a/W$, B is the thickness, W is the width, a is the notch depth, S is the support span, and P is the load. Compressive tests were conducted at room temperature (MTS 810) in air and 1300 ºC (Instron universal tester) in vacuum, respectively, with a sample dimension of 3×3×4.5 mm^3 and a strain rate of 10^{-3}/s. The ultimate compressive strength was determined from stress-strain curves.

3. Results and discussion

XRD of HEA0C, HEA25C, HEA50C, HEA75C and HEA100C samples are shown in **Fig. 1a**. XRD of HEA100C is consistent with the previous report [29]. HEA100C and HEA75C samples have a single-phase HEC with a rock-salt B1 crystal structure (space group $Fm\bar{3}m$) of transition metal carbide (MC). The lattice parameter of HEA100C was calculated as a=0.4495 nm. HEA0C sample contains a HEA with body-centered cubic (BCC, lattice parameter a=0.3311 nm) structure as the major phase while the impurity peaks were identified as Zr_3O (space group P6322) by Jade Software. HEA50C and HEA25C samples consist of two phases, including both B1 HEC and BCC HEA (**Figs. 1a** and **1b**). Notably, the

XRD spectrum showed no detectable iron (Fe) peaks, indicating the absence of steel contamination in the milled HEA50C powder.

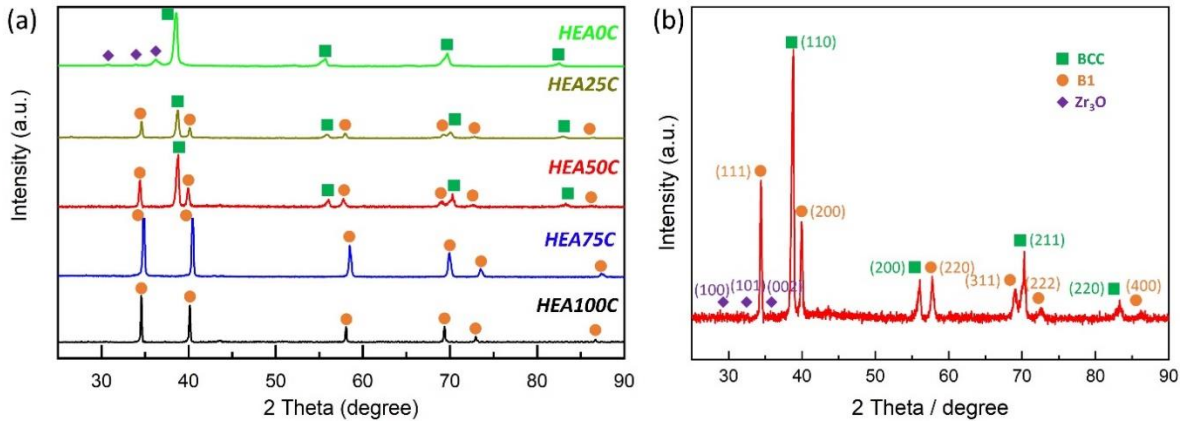


Fig. 1. (a) XRD of HEA0C, HEA25C, HEA50C, HEA75C and HEA100C samples; (b) XRD results reveal the phases in the HEA50C sample: HEA (BCC structure), HEC (B1 structure), and Zr_3O impurity.

SEM images of the HEA0C, HEA50C, and HEA100C samples are presented in **Fig. 2**. The chemical composition range of HEA0C and HEA50C according to the EDS analysis is listed in **Table 1**. In the HEA0C sample (**Fig. 2a**), the dark grey contrast (about 40 vol.%) is Zr- and Ti-rich while the light grey contrast (about 60 vol.%) is slightly enriched with Ta. This may indicate element segregations in HEA although it is a single phase of BCC structure according to XRD (Fig. 1a). In the HEA25C sample (**Fig. 2b**), the dark grey region (approximately 25.3 vol.%) represents the Zr-rich HEC phase, while the light grey region (about 74.7 vol.%) corresponds to the Ta- and Nb-rich HEA phase. In the HEA50C sample (**Fig. 2c**), the dark grey region (51.5 vol.%) is Zr-rich HEC phase whereas the light grey region is Ta- and Nb-rich HEA phase. The HEA75C sample (**Fig. 2d**) predominantly consists of dark grey regions of the HEC phase. The HEA100C sample (**Fig. 2e**) has a homogenous single contrast. The average grain sizes of both HEA0C and HEA100C are 0.63 and 20 µm, respectively (**Table 2**). In the HEA50C sample, the average grain size is 1.41 µm, in which HEC phase has an average grain size of 1.20 µm while the HEA phase has an average grain size of 1.64 µm.

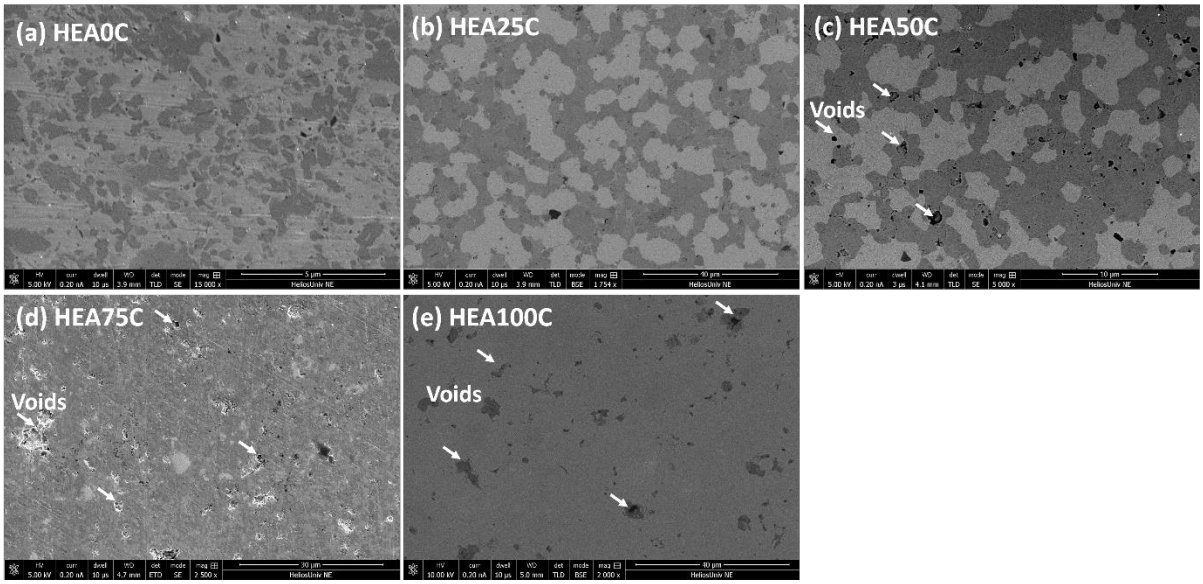


Fig. 2. SEM images of the polished surfaces of the (a) HEA0C, (b) HEA25C, (c) HEA50C, (d) HEA75C, and HEA100C samples. Black contrast (arrowed) indicates porosity (voids).

Table 1. Chemical compositions in the HEA0C and HEA50C samples (at. %).

Elements	HEA0C		HEA50C	
	Dark grey	Light grey	HEA phase	HEC phase
C	-	-	13.4~18.7	36.8~49.6
Zr	41.3	23.6	10.0~11.1	27.9~28.3
Ti	29.1	23.3	20.5~22.5	21.2~22.0
Ta	17.3	30.4	34.7~35.5	8.2~9.1
Nb	12.3	22.7	32.2~34.1	5.9~7.2

TiTaNbZr HEA fabricated by arc melting has been reported in the literature. Qian et al., [35,36] reported the formation of a single phase with BCC structure by arc melting, in which the sample was rapidly cooled from melting to room temperature. In contrast, Liu et al., [37] fabricated a dual-phase TiTaNbZr HEA consisting of Zr- and Ti-rich HCP phase and Nb- and Ta-rich BCC phase. The fabrication process involved arc melting, followed by homogenization at 1100 °C for 24 h, and finally water quenching. According to both literatures, it is likely that the phase transformation of a single-phase BCC may occur in TiTaNbZr HEA at 1100 °C, during which two separate phases (HCP and BCC) were formed. In this study, because SPS is a solid-state process in which the temperature (1500 ℃) is below

the melting point but much higher than 1100 ºC, a single-phase BCC HEA was formed but the element segregations (Table 1) may result from the incomplete alloying of Ti, Ta, Nb, and Zr metal element powders. Incomplete alloying was also observed during SPS of other refractory HEAs such as CrMoNbTiW [38] and $Nb_{42}Mo_{20}Ti_{13}Cr_{12}V_{12}Ta_1$ [39].

To further reveal the element and phase distributions in the HEA50C sample, EDS analysis in TEM was conducted. **Fig. 3a** is a high-angle annual dark field (HAADF) image in which the light grey contrast indicates higher average atomic number and the dark grey region lower atomic number. HAADF image reveals the coexistence of the HEC and HEA phases with a well-defined interface between them. It displays a clear boundary and intimate contact between the two phases, indicating a distinct interfacial region. EDS mapping analysis (**Fig. 3b** to **3g**) suggests that the light grey contrast region is enriched with Nb and Ta, while the dark grey region is enriched with C, Ti, and Zr, suggesting that the light grey contrast is the HEA phase, and the dark grey contrast is the HEC phase. EDS line scanning (**Fig. 3h**) across the interface of both phases show that the HEA phase has ~9 at.% C, ~9 at.% O, ~11 at.% Ti, ~31 at.% Ta, ~31 at.% Nb, and ~8 at.% Zr, while the HEC phase has ~13 at.% C, ~10 at.% O, ~19 at.% Ti, ~13 at.% Ta, ~6 at.% Nb and ~38 at.% Zr. Nevertheless, it is important to note that the quantitative chemical compositions in the EDS analysis are not accurate for low-Z elements such as oxygen (O) or carbon (C). Both the HEA and HEC phases in HEA50C are single-phase non-equiatomic solid solutions [40]. In the microstructure analysis, a small portion of impurity inclusions were also observed, highlighted by yellow arrows, which exhibited deficiencies of Ti and C. Based on EDS mapping (Fig. 3d and 3g) and XRD (Fig. 1b) analysis, these inclusions were very likely Zr_3O. The slight contrast differences among the HEC grains observed in the HAADF image (Fig. 3a) may be attributed to variations in crystal orientations.

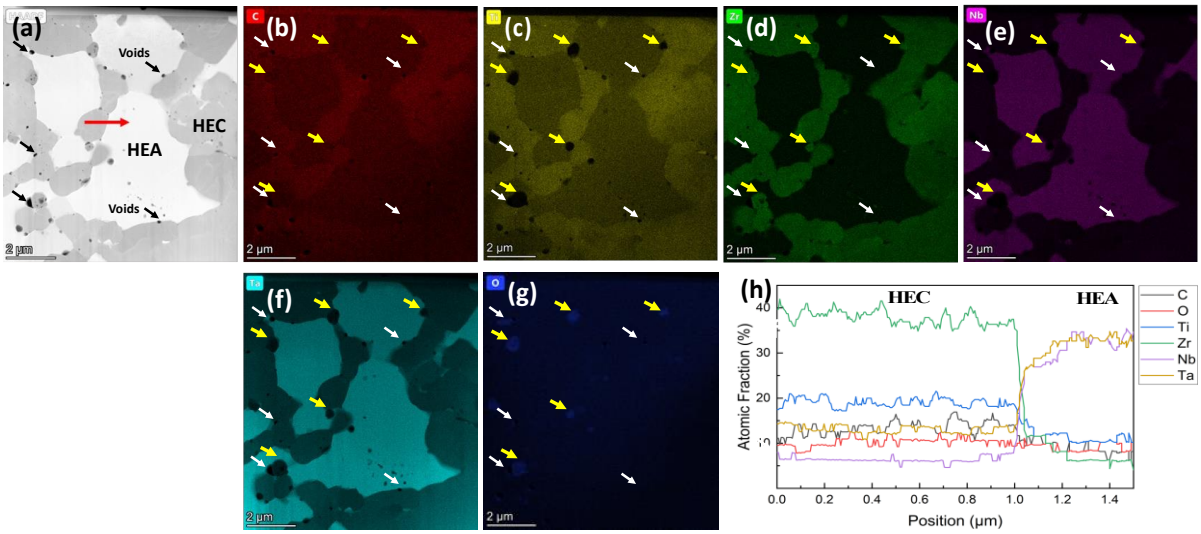


Fig. 3. (a) HAADF of HEA50C; (b)-(g) EDS element mapping analysis and (h) EDS line scanning along the red arrow in (a). Black contrast (light grey arrowed) indicates porosity. Yellow arrows indicate small Zr_3O inclusions.

The formation mechanisms of both HEA and HEC phases in HEA50C may need more investigations. Previous research from our team suggested that a single-phase solid solution was not formed in the HEC precursor powder after ball milling at 250 rpm for 6 h, which is still a mixture of TiC, TaC, NbC, and ZrC [13,40]. In contrast, a single-phase solid solution was possible to be formed in the HEA precursor powder after ball milling at 400 rpm for 30 h. When the HEA and HEC precursor powders were mixed, ball milled, and consolidated by SPS at 1500 ºC, the solid solution of the HEC phase was formed. Compared to the HEA phase, the HEC phase has more Zr, which is consistent with the order of Gibbs free energy of ZrC (-339 $J \cdot K^{-1}mol^{-1}$) < TiC (-306 $J \cdot K^{-1}mol^{-1}$) < TaC (-300 $J \cdot K^{-1}mol^{-1}$) < NbC (-286 $J \cdot K^{-1}mol^{-1}$). The phase stability of the HECs may be influenced by chemical potential, which is the partial derivative of the Gibbs free energy with respect to a particular component [9,16]. The atomic diffusion of Zr from HEA to HEC phase is driven by the chemical potential, as atoms tend to redistribute themselves to minimize the overall Gibbs free energy. On the other hand, C was detected both in the HEA and HEC phases, suggesting the possible diffusion of C from the HEC to HEA phase.

The bulk density of the HEMCC samples were measured by the Archimedes method and listed in **Table 2**, which shows that the density was decreased with more HEC phase, from 8.72 of HEA0C to 8.02 g/cm^3 of HEA100C. It is noted that porosity (0.2 to 0.5 μm) is present in the SEM and TEM images (**Figs.** 2 and 3) with a black contrast. The porosity in each HEMCC sample was measured from the SEM and TEM images, which are in the range of 1.7 to 2.8 vol.%. Furthermore, voids were observed at the interphase between the HEA and HEC

phases according to the TEM image (Fig. 3). The coefficients of thermal expansion (CTE) for HEA and HEC phases have significant differences. The CTE for HEA ranges from approximately 2.178 × 10^{-5} K^{-1} at 1700 K to 1.786 × 10^{-5} K^{-1} at 300 K [41], while for HEC, it varies from 6 to 7 × 10^{-6} K^{-1} at 300 K [40,42]. Thus, some voids may be generated at the HEA/HEC interphases due to the different shrinkage rates during the cooling process.

Table 2. Bulk density and mechanical properties of the HEMCC samples.

	Theoretical density ($g \cdot cm^{-3}$)	Bulk density ($g \cdot cm^{-3}$)	Porosity (%)	Average grain size (μm)	Vickers Hardness (GPa)	Flexural strength (MPa)	Fracture toughness ($MPa \cdot m^{1/2}$)	Compressive strength (MPa)
HEA0C	8.91	8.72	2.1	0.63±1.07	6.15±0.19	455±26	7.97±0.40	1691 (25 ℃) 58 (1300 ℃)
HEA25C	8.80	8.63	2.0	1.29±0.70	6.49±0.38	-	-	-
HEA50C	8.69	8.55	1.7	1.41±1.69	9.12±0.36	541±48	6.93±0.27	2423 (25 ℃) 275 (1300 ℃)
HEA75C	8.58	8.34	2.8	4.28±6.90	18.03±1.23	-	-	-
HEA100C	8.47	8.02	5.4	20.0±11.2	17.70±2.00	343±15	4.70±0.17	-

The mechanical properties of the HEMCC samples are also summarized in **Table 2**. Small-scale hardness tests were performed first due to the ease of sample preparation. The Vickers hardness of HEA100C (17.7 GPa) was much higher than HEA0C (6.15 GPa) and HEA50C (9.12 GPa). **Figs. 4a** to **4d** are SEM images of the Vickers indentations created by the same load of 10 N on each HEMCC sample. The indentation size decreases from HEA0C to HEA75C, suggesting an increase in the Vickers hardness. Cracks were generated from the corners of the Vickers indentations on the HEA75C sample, while HEA0C, HEA25C, and HEA50C do not have obvious cracks. **Fig. 4e** shows the Vickers indentation on HEA50C at a higher magnification, in which small cracks were initiated from the corners of the Vickers indentation, propagated in the HEC phase, and then arrested at HEC/HEA interface in HEA50C. No crack deflection along the HEC/HEA interface was observed, suggesting a strong interfacial strength [44,45]. Therefore, these findings indicate that although crack initiation can occur in the HEC phase, the HEA/HEC interfaces and HEA phase can provide a high resistance to crack growth. This provides an effective mechanism for improving the facture toughness of HEA50C. In addition, because HEA has a higher CET than HEC, tensile residual stresses may be developed in the HEA phase while compressive residual stress in the HEC phase upon cooling following the high-temperature processing (1500 ℃). The compressive residual stress in the HEC phase may cause a reduction of driving force for crack propagation. The HEA phase can accommodate plastic deformation and absorb elastic energy associated with crack propagation, leading to crack arrest at the HEA/HEC interface.

Similar crack arrest mechanisms have been observed in other metal/ceramic composites, such as Ti/Al_2O_3 and Al/Al_2O_3 composites [46–48].

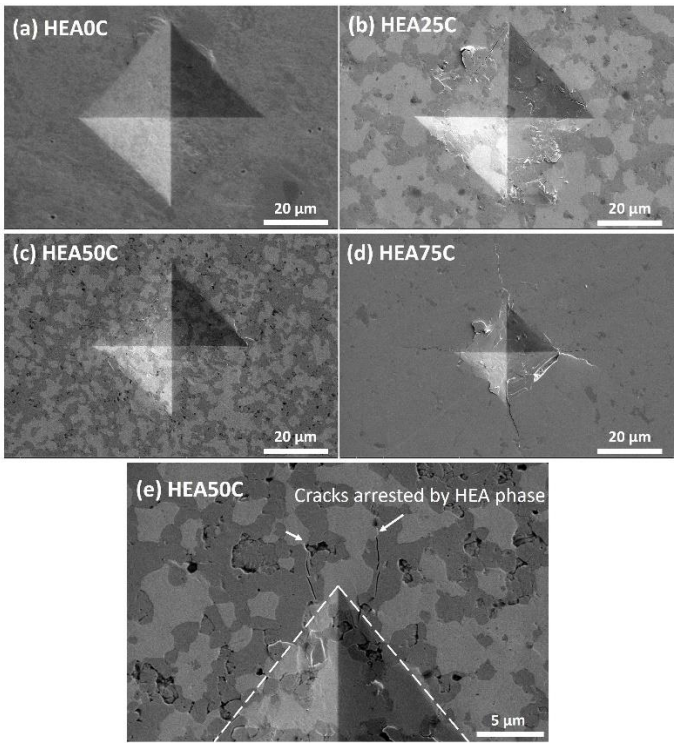


Fig. 4. SEM images of the Vickers indentations and corner cracks in each HEMCC sample: (a) HEA0C; (b) HEA25C; (c) HEA50C; and (d) HEA75C. (e) Crack propagation near a corner of the Vickers indentation in HEA50C.

Nanoindentation of HEA50C sample was conducted to further reveal the local mechanical properties. **Fig. 5** presents mapping of elastic modulus and nanohardness in HEA50C using the grid nanoindentation technique, which revealed the significant difference between the HEA and HEC phases. The elastic modulus (281±9.0 GPa) of the HEC phase is 61% higher than that (174±15 GPa) of the HEA phase. The nanohardness (42.7±3.9 GPa) of the HEC phase is 4.2 times of that of the HEA phase (10.0±1.0 GPa).

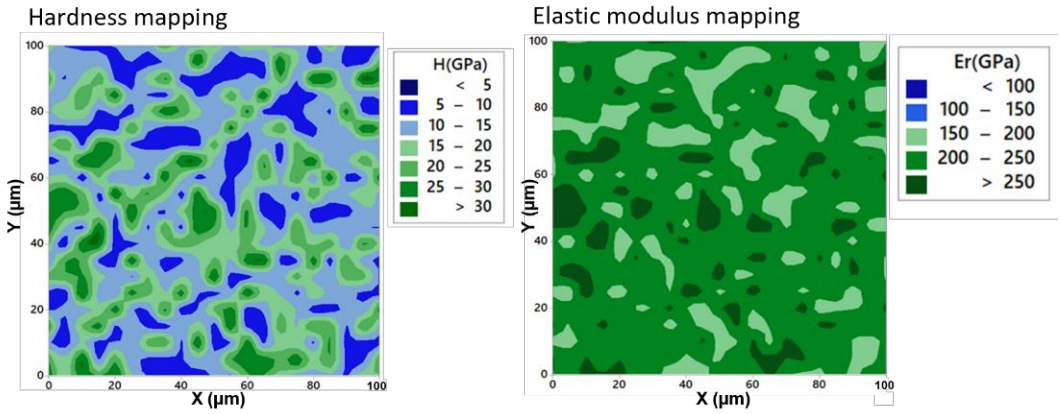


Fig. 5. Mapping of nanohardness and elastic modulus in HEA50C

Macroscale mechanical tests were conducted to further evaluate the mechanical performance of HEMCC, which were mostly conducted at room temperature except for the compressive tests at both room temperature and 1300 ºC. Interestingly, the flexural strength of HEA50C (541±48 MPa) was 19% and 58% higher than those of HEA0C (455±26 MPa) and HEA100C (343±15 MPa), respectively (**Table 2**). The fracture toughness is decreased with more HEC phase, from 7.97±0.40 MPa·$m^{1/2}$ of HEA0C to 4.70±0.17 MPa·$m^{1/2}$ of HEA100C. Fracture surfaces of HEA0C, HEA50C, and HEA100C are shown in **Fig. 6**. The fracture mode of the HEA0C sample is mainly transgranular fracture (**Fig. 6a**), while that of HEA100C is mainly transgranular cleavage in large grains and intergranular fracture in smaller grains (**Fig. 6b**). The fracture mode of HEA50C (**Fig. 6c**) is a combination of transgranular and intergranular fractures, which is indicative of brittle fracture behavior.

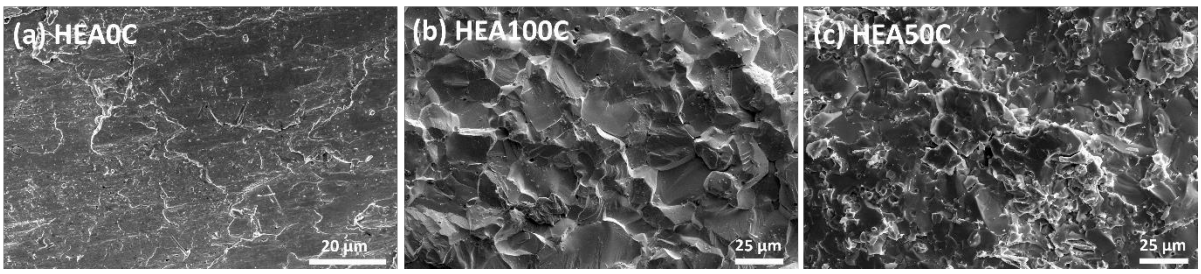


Fig. 6. Fracture surfaces of the (a) HEA0C, (b) HEA100C, and (c) HEA50C samples.

Overall, HEA50C shows a favorable combination of flexural strength (541±48 MPa) and fracture toughness (6.93±0.27 MPa·$m^{1/2}$) at room temperature. Notably, these mechanical properties surpass those reported for most other HEAs, HECs or composites when utilizing the standard sub-sized specimens and SENB test method., such as (Ta,Zr,Nb)C with a

flexural strength of 460 MPa and fracture toughness of 2.9 MPa·$m^{1/2}$ [51], $C_f/BN_i/(TiZrHfNbTa)C$-SiC_m with a flexural strength of 269 MPa [52], $V_{20}Nb_{20}Mo_{20}Ta_{20}W_{20}$ with a flexural strength of 378 MPa [53], (VNbTaMoW)C with a flexural strength of 192 MPa and fracture toughness of 3.34 MPa·$m^{1/2}$ [54], and Al_2O_3/(NbTaMoW)C with a flexural strength of 530 MPa and fracture toughness of 4.5 MPa·$m^{1/2}$ [55]. Compared to HEA0C (100% HEA phase), HEA50C has a higher flexural strength and lower fracture toughness, which can be attributed to the strengthening effect of strong but brittle HEC phase in HEA50C. Compared to HEA100C (100% HEC phase), HEA50C has a higher flexural strength and fracture toughness, which may be attributed to the smaller grain size (1.41 μm) of HEA50C than that of HEA100C (20 μm) as well as the HEA/HEC interface that provide crack growth resistance (see **Fig.** 5e).

Fig. 7 shows the stress-strain curves of HEA0C and HEA50C during compression tests at 1300 ºC. The ultimate compressive strengths of HEA0C are 1691 MPa at 25 ºC and 58 MPa at 1300 ºC (**Table 2**). With the addition of 50% HEC, the ultimate compressive strength of HEA50C had a significant increase to 2423 MPa at 25 ºC and 275 MPa at 1300 ºC. Such significant improvement in the high-temperature strength is attributed to the strengthening effect of the HEC phase, which can retain its strength to high temperatures (up to 1800 ºC [10]). The ultimate compressive strength of HEA50C at 1300 ºC (275 MPa) is higher than that of most existing refractory HEAs (i.e. 253 MPa for $Mo_{25}Nb_{50}V_{20}W_5$ [56]) and other refractor alloys such as C-103 (<100 MPa) [57] or TZM (200 MPa) [58] at 1300 ºC. It is also noted that after its ultimate strength, the HEA50C sample still experienced plastic deformation with a plastic strain over 23% (Fig. 7). The high strength and ductility of HEA50C at 1300 ºC may indicate that it is a promising structural material for high-temperature extreme environments, such as in gas turbine blade applications.

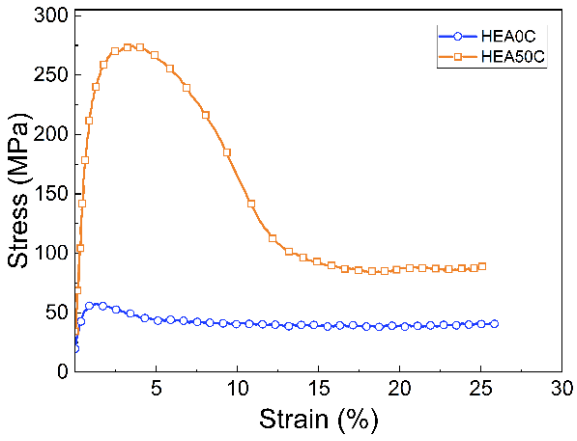


Fig. 7 Compressive stress-strain curves for HEA0C and HEA50C at 1300 ºC.

4. Conclusions

The novel HEMCC system of TiTaNbZr-(TiTaNbZr)C was developed by a powder metallurgy process that combined high-energy ball milling and SPS. In its microstructure, the Ta- and Nb-rich HEA phase has BCC, while the Zr-rich HEC phase has rock-salt B1 crystal structure. With the increase of the HEC phase in HEMCC, the hardness is enhanced, the density and fracture toughness are decreased. HEA50C shows a good combination of flexural strength (541±48 MPa) and fracture toughness (6.93±0.27 $MPa \cdot m^{1/2}$) at room temperature and a high compressive strength at 1300 ºC (275 MPa). The homogeneous distribution of ductile HEA and strong HEC phases in microstructures, small grain size, and crack arrest at the HEA/HEC interface, may lead to the excellent mechanical properties of HEMCC in extreme environments.

Acknowledgment

The information, data, or work presented herein was funded in part by the Advanced Research Projects Agency-Energy (ARPA-E), U.S. Department of Energy, under Award Number DE-AR0001428. The views and opinions of authors expressed herein do not necessarily state or reflect those of the United States Government or any agency thereof. The research was performed in part in the Nebraska Nanoscale Facility: National Nanotechnology Coordinated Infrastructure and the Nebraska Center for Materials and Nanoscience (and/or NERCF), which are supported by the National Science Foundation under Award ECCS: 2025298, and the Nebraska Research Initiative. The authors also acknowledge the U.S. Department of Energy, Office of Nuclear Energy under DOE Idaho Operations Office Contract DE-AC07-051D14517, for use of the resources as part of Nuclear Science User Facilities.

References:

[1] H. Long, S. Mao, Y. Liu, Z. Zhang, X. Han, Microstructural and compositional design of Ni-based single crystalline superalloys — A review, J. Alloys Compd. 743 (2018) 203–220. https://doi.org/10.1016/j.jallcom.2018.01.224.

[2] W.-Y. Kim, H. Tanaka, M.-S. Kim, S. Hanada, High temperature strength and room temperature fracture toughness of Nb–Mo–W refractory alloys with and without carbide dispersoids, Mater. Sci. Eng. A. 346 (2003) 65–74. https://doi.org/10.1016/S0921-5093(02)00515-4.

[3] B. Riccardi, L. Giancarli, A. Hasegawa, Y. Katoh, A. Kohyama, R.H. Jones, L.L. Snead, Issues and advances in SiCf/SiC composites development for fusion reactors, J. Nucl. Mater. 329–333 (2004) 56–65. https://doi.org/10.1016/j.jnucmat.2004.04.002.

[4] R. Schafrik, R. Sprague, Superalloy Technology - A Perspective on Critical Innovations for Turbine Engines, Key Eng. Mater. 380 (2008) 113–134. https://doi.org/10.4028/www.scientific.net/KEM.380.113.

[5] V.V. Satya Prasad, R.G. Baligidad, A.A. Gokhale, Niobium and Other High Temperature Refractory Metals for Aerospace Applications, in: N.E. Prasad, R.J.H. Wanhill (Eds.), Aerosp. Mater. Mater. Technol. Vol. 1 Aerosp. Mater., Springer, Singapore, 2017: pp. 267–288. https://doi.org/10.1007/978-981-10-2134-3_12.

[6] R. Swadźba, High temperature oxidation behavior of C103 alloy with boronized and siliconized coatings during 1000 h at 1100 °C in air, Surf. Coat. Technol. 370 (2019) 331–339. https://doi.org/10.1016/j.surfcoat.2019.04.019.

[7] G.R. Smolik, D.A. Petti, S.T. Schuetz, Oxidation and volatilization of TZM alloy in air, J. Nucl. Mater. 283–287 (2000) 1458–1462. https://doi.org/10.1016/S0022-3115(00)00303-2.

[8] M.S. El-Genk, J.-M. Tournier, A review of refractory metal alloys and mechanically alloyed-oxide dispersion strengthened steels for space nuclear power systems, J. Nucl. Mater. 340 (2005) 93–112. https://doi.org/10.1016/j.jnucmat.2004.10.118.

[9] F. Wang, F. Monteverde, B. Cui, Will high-entropy carbides and borides be enabling materials for extreme environments?, Int. J. Extreme Manuf. 5 (2023) 022002. https://doi.org/10.1088/2631-7990/acbd6e.

[10] M.-H. Tsai, J.-W. Yeh, High-Entropy Alloys: A Critical Review, Mater. Res. Lett. 2 (2014) 107–123. https://doi.org/10.1080/21663831.2014.912690.

[11] X. Zhang, F. Wang, X. Yan, X.-Z. Li, K. Hattar, B. Cui, Nanostructured Oxide-Dispersion-Strengthened CoCrFeMnNi High-Entropy Alloys with High Thermal Stability, Adv. Eng. Mater. 23 (2021) 2100291. https://doi.org/10.1002/adem.202100291.

[12] X.B. Feng, J.Y. Zhang, Y.Q. Wang, Z.Q. Hou, K. Wu, G. Liu, J. Sun, Size effects on the mechanical properties of nanocrystalline NbMoTaW refractory high entropy alloy thin films, Int. J. Plast. 95 (2017) 264–277. https://doi.org/10.1016/j.ijplas.2017.04.013.

[13] X. Yan, L. Constantin, Y. Lu, J.-F. Silvain, M. Nastasi, B. Cui, (Hf0.2Zr0.2Ta0.2Nb0.2Ti0.2)C high-entropy ceramics with low thermal conductivity, J. Am. Ceram. Soc. 101 (2018) 4486–4491. https://doi.org/10.1111/jace.15779.

[14] F. Wang, X. Zhang, X. Yan, Y. Lu, M. Nastasi, Y. Chen, B. Cui, The effect of submicron grain size on thermal stability and mechanical properties of high-entropy carbide ceramics, J. Am. Ceram. Soc. 103 (2020) 4463–4472. https://doi.org/10.1111/jace.17103.

[15] S. Barbarossa, R. Orrù, V. Cannillo, A. Iacomini, S. Garroni, M. Murgia, G. Cao, Fabrication and Characterization of Quinary High Entropy-Ultra-High Temperature Diborides, Ceramics. 4 (2021) 108–120. https://doi.org/10.3390/ceramics4020010.

[16] X. Tang, G.B. Thompson, K. Ma, C.R. Weinberger, The role of entropy and enthalpy in high entropy carbides, Comput. Mater. Sci. 210 (2022) 111474. https://doi.org/10.1016/j.commatsci.2022.111474.

[17] A.J. Wright, Q. Wang, C. Huang, A. Nieto, R. Chen, J. Luo, From high-entropy ceramics to compositionally-complex ceramics: A case study of fluorite oxides, J. Eur. Ceram. Soc. 40 (2020) 2120–2129. https://doi.org/10.1016/j.jeurceramsoc.2020.01.015.

[18] P. Lu, J.E. Saal, G.B. Olson, T. Li, S. Sahu, O.J. Swanson, G.S. Frankel, A.Y. Gerard, J.R. Scully, Computational design and initial corrosion assessment of a series of non-equimolar high entropy alloys, Scr. Mater. 172 (2019) 12–16. https://doi.org/10.1016/j.scriptamat.2019.07.003.

[19] A.J. Wright, J. Luo, A step forward from high-entropy ceramics to compositionally complex ceramics: a new perspective, J. Mater. Sci. 55 (2020) 9812–9827. https://doi.org/10.1007/s10853-020-04583-w.

[20] Y.D. Wu, Y.H. Cai, T. Wang, J.J. Si, J. Zhu, Y.D. Wang, X.D. Hui, A refractory Hf25Nb25Ti25Zr25 high-entropy alloy with excellent structural stability and tensile properties, Mater. Lett. 130 (2014) 277–280. https://doi.org/10.1016/j.matlet.2014.05.134.

[21] B. Yin, F. Maresca, W.A. Curtin, Vanadium is an optimal element for strengthening in both fcc and bcc high-entropy alloys, Acta Mater. 188 (2020) 486–491. https://doi.org/10.1016/j.actamat.2020.01.062.

[22] O.N. Senkov, G.B. Wilks, J.M. Scott, D.B. Miracle, Mechanical properties of Nb25Mo25Ta25W25 and V20Nb20Mo20Ta20W20 refractory high entropy alloys, Intermetallics. 19 (2011) 698–706. https://doi.org/10.1016/j.intermet.2011.01.004.

[23] L. Feng, W.-T. Chen, W.G. Fahrenholtz, G.E. Hilmas, Strength of single-phase high-entropy carbide ceramics up to 2300°C, J. Am. Ceram. Soc. 104 (2021) 419–427. https://doi.org/10.1111/jace.17443.

[24] Q. Wei, Q. Shen, J. Zhang, Y. Zhang, G. Luo, L. Zhang, Microstructure evolution, mechanical properties and strengthening mechanism of refractory high-entropy alloy matrix composites with addition of TaC, J. Alloys Compd. 777 (2019) 1168–1175. https://doi.org/10.1016/j.jallcom.2018.11.111.

[25] P.L. Zhou, D.H. Xiao, P.F. Zhou, T.C. Yuan, Microstructure and properties of ultrafine grained AlCrFeCoNi/WC cemented carbides, Ceram. Int. 44 (2018) 17160–17166. https://doi.org/10.1016/j.ceramint.2018.06.171.

[26] M. Zhang, R. Li, T. Yuan, X. Feng, L. Li, S. Xie, Q. Weng, Densification and properties of B4C-based ceramics with CrMnFeCoNi high entropy alloy as a sintering aid by spark plasma sintering, Powder Technol. 343 (2019) 58–67. https://doi.org/10.1016/j.powtec.2018.11.005.

[27] Y. Arai, M. Saito, Y. Kogo, Material design for TiZrHfNbTaBx: A boundary material of refractory high-entropy alloys and ceramics, MRS Adv. 7 (2022) 848–852. https://doi.org/10.1557/s43580-022-00337-9.

[28] B. Cui, F. Wang, High-entropy metal/ceramic composite materials for harsh environments, WO2022204556A1, 2022. https://patents.google.com/patent/WO2022204556A1/en?oq=WO2022%2f204556 (accessed May 5, 2023).

[29] F. Wang, X. Yan, T. Wang, Y. Wu, L. Shao, M. Nastasi, Y. Lu, B. Cui, Irradiation damage in (Zr0.25Ta0.25Nb0.25Ti0.25)C high-entropy carbide ceramics, Acta Mater. 195 (2020) 739–749. https://doi.org/10.1016/j.actamat.2020.06.011.

[30] X. Zhang, M. Khedmati, Y.-R. Kim, H.-S. Shin, J. Lee, Y.-J. Kim, B. Cui, Microstructure evolution during spark plasma sintering of FJS-1 lunar soil simulant, J. Am. Ceram. Soc. 103 (2020) 899–911. https://doi.org/10.1111/jace.16808.

[31] P. Sudharshan Phani, W.C. Oliver, A critical assessment of the effect of indentation spacing on the measurement of hardness and modulus using instrumented indentation testing, Mater. Des. 164 (2019) 107563. https://doi.org/10.1016/j.matdes.2018.107563.

[32] Z. Zhao, H. Xiang, F.-Z. Dai, Z. Peng, Y. Zhou, (La0.2Ce0.2Nd0.2Sm0.2Eu0.2)2Zr2O7: A novel high-entropy ceramic with low thermal conductivity and sluggish grain growth rate, J. Mater. Sci. Technol. 35 (2019) 2647–2651. https://doi.org/10.1016/j.jmst.2019.05.054.

[33] G.A. Sweet, M. Brochu, R.L. Hexemer, I.W. Donaldson, D.P. Bishop, Consolidation of aluminum-based metal matrix composites via spark plasma sintering, Mater. Sci. Eng. A. 648 (2015) 123–133. https://doi.org/10.1016/j.msea.2015.09.027.

[34] S.R. Oke, O.E. Falodun, A. Bayode, U.S. Anamu, P.A. Olubambi, Phase prediction, densification, and microstructure of AlCrFeNi(TiO2)x high entropy alloy composite fabricated by spark plasma sintering, J. Alloys Compd. 968 (2023) 172030. https://doi.org/10.1016/j.jallcom.2023.172030.

[35] V.T. Nguyen, M. Qian, Z. Shi, X.Q. Tran, D.M. Fabijanic, J. Joseph, D.D. Qu, S. Matsumura, C. Zhang, F. Zhang, J. Zou, Cuboid-like nanostructure strengthened equiatomic Ti–Zr–Nb–Ta medium entropy alloy, Mater. Sci. Eng. A. 798 (2020) 140169. https://doi.org/10.1016/j.msea.2020.140169.

[36] V.T. Nguyen, M. Qian, Z. Shi, T. Song, L. Huang, J. Zou, A novel quaternary equiatomic Ti-Zr-Nb-Ta medium entropy alloy (MEA), Intermetallics. 101 (2018) 39–43. https://doi.org/10.1016/j.intermet.2018.07.008.

[37] T.-Y. Liu, J.C. Huang, W.-S. Chuang, H.-S. Chou, J.-Y. Wei, C.-Y. Chao, Y.-C. Liao, J.S.C. Jang, Spinodal Decomposition and Mechanical Response of a TiZrNbTa High-Entropy Alloy, Materials. 12 (2019) 3508. https://doi.org/10.3390/ma12213508.

[38] L. Raman, G. Karthick, K. Guruvidyathri, D. Fabijanic, S.V.S.N. Murty, B.S. Murty, R.S. Kottada, Influence of processing route on the alloying behavior, microstructural evolution and thermal stability of CrMoNbTiW refractory high-entropy alloy, J. Mater. Res. 35 (2020) 1556–1571. https://doi.org/10.1557/jmr.2020.128.

[39] B. Kang, T. Kong, A. Raza, H.J. Ryu, S.H. Hong, Fabrication, microstructure and mechanical property of a novel Nb-rich refractory high-entropy alloy strengthened by in-situ formation of dispersoids, Int. J. Refract. Met. Hard Mater. 81 (2019) 15–20. https://doi.org/10.1016/j.ijrmhm.2019.02.009.

[40] X. Zhang, N. Li, X. Chen, M. Stroup, Y. Lu, B. Cui, Direct selective laser sintering of high-entropy carbide ceramics, J. Mater. Res. 38 (2023) 187–197. https://doi.org/10.1557/s43578-022-00766-0.

[41] M. Yang, L. Shao, J.-M. Duan, X.-T. Chen, B.-Y. Tang, Temperature dependence of mechanical and thermodynamic properties of Ti(25+x)Zr25Nb25Ta(25-x) ($x \leq 20$) refractory high entropy alloys: Influences of substitution of Ti for Ta, Phys. B Condens. Matter. 606 (2021) 412851. https://doi.org/10.1016/j.physb.2021.412851.

[42] S. Jiang, L. Shao, T.-W. Fan, J.-M. Duan, X.-T. Chen, B.-Y. Tang, Elastic and thermodynamic properties of high entropy carbide (HfTaZrTi)C and (HfTaZrNb)C from ab initio investigation, Ceram. Int. 46 (2020) 15104–15112. https://doi.org/10.1016/j.ceramint.2020.03.045.

[43] K. Xiong, B.-W. Wang, Z.-P. Sun, W. Li, C.-C. Jin, S.-M. Zhang, S.-Y. Xu, L. Guo, Y. Mao, Frist-principles prediction of elastic, electronic, and thermodynamic properties of high entropy carbide ceramic (TiZrNbTa)C, Rare Met. 41 (2022) 1002–1014. https://doi.org/10.1007/s12598-021-01834-w.

[44] S.G. Warrier, B.S. Majumdar, D.B. Miracle, Interface effects on crack deflection and bridging during fatigue crack growth of titanium matrix composites, Acta Mater. 45 (1997) 4969–4980. https://doi.org/10.1016/S1359-6454(97)00179-1.

[45] N. Carrère, E. Martin, J. Lamon, The influence of the interphase and associated interfaces on the deflection of matrix cracks in ceramic matrix composites, Compos. Part Appl. Sci. Manuf. 31 (2000) 1179–1190. https://doi.org/10.1016/S1359-835X(00)00095-6.

[46] C. Wu, Y. Li, Z. Wang, Evolution and mechanism of crack propagation method of interface in laminated Ti/Al2O3 composite, J. Alloys Compd. 665 (2016) 37–41. https://doi.org/10.1016/j.jallcom.2016.01.041.

[47] C. Ferraro, S. Meille, J. Réthoré, N. Ni, J. Chevalier, E. Saiz, Strong and tough metal/ceramic micro-laminates, Acta Mater. 144 (2018) 202–215. https://doi.org/10.1016/j.actamat.2017.10.059.

[48] A. Bandyopadhyay, K. Das, J. Marusich, S. Onagoruwa, Application of fused deposition in controlled microstructure metal- ceramic composites, Rapid Prototyp. J. 12 (2006) 121–128. https://doi.org/10.1108/13552540610670690.

[49] P. Agrawal, C.T. Sun, Fracture in metal–ceramic composites, Compos. Sci. Technol. 64 (2004) 1167–1178. https://doi.org/10.1016/j.compscitech.2003.09.026.

[50] D. Kozic, H.-P. Gänser, R. Brunner, D. Kiener, T. Antretter, O. Kolednik, Crack arrest in thin metallic film stacks due to material- and residual stress inhomogeneities, Thin Solid Films. 668 (2018) 14–22. https://doi.org/10.1016/j.tsf.2018.10.014.

[51] D. Demirskyi, H. Borodianska, T.S. Suzuki, Y. Sakka, K. Yoshimi, O. Vasylkiv, High-temperature flexural strength performance of ternary high-entropy carbide consolidated via spark plasma sintering of TaC, ZrC and NbC, Scr. Mater. 164 (2019) 12–16. https://doi.org/10.1016/j.scriptamat.2019.01.024.

[52] L. Zhang, W. Wang, N. Zhou, X. Dong, F. Yuan, R. He, Low temperature fabrication of Cf/BNi/(Ti0.2Zr0.2Hf0.2Nb0.2Ta0.2)C-SiCm high entropy ceramic matrix composite by slurry coating and laminating combined with precursor infiltration and pyrolysis, J. Eur. Ceram. Soc. 42 (2022) 3099–3106. https://doi.org/10.1016/j.jeurceramsoc.2022.02.021.

[53] S.J. Wu, X.D. Wang, J.T. Lu, R.T. Qu, Z.F. Zhang, Room-Temperature Mechanical Properties of V20Nb20Mo20Ta20W20 High-Entropy Alloy, Adv. Eng. Mater. 20 (2018) 1800028. https://doi.org/10.1002/adem.201800028.

[54] D. Liu, A. Zhang, J. Jia, J. Meng, B. Su, Phase evolution and properties of (VNbTaMoW)C high entropy carbide prepared by reaction synthesis, J. Eur. Ceram. Soc. 40 (2020) 2746–2751. https://doi.org/10.1016/j.jeurceramsoc.2020.03.020.

[55] D. Liu, A. Zhang, J. Jia, J. Han, J. Zhang, J. Meng, A novel in-situ exothermic assisted sintering high entropy Al2O3/(NbTaMoW)C composites: Microstructure and mechanical properties, Compos. Part B Eng. 212 (2021) 108681. https://doi.org/10.1016/j.compositesb.2021.108681.

[56] B. Vela, C. Acemi, P. Singh, T. Kirk, W. Trehern, E. Norris, D.D. Johnson, I. Karaman, R. Arróyave, High-throughput exploration of the WMoVTaNbAl refractory multi-principal-element alloys under multiple-property constraints, Acta Mater. 248 (2023) 118784. https://doi.org/10.1016/j.actamat.2023.118784.

[57] C. Wojcik, Chang, W., Thermomechanical processing and properties of niobium alloys, Int. Symp. Niobium 2001. (2001) 163–173.

[58] K. Yoshimi, J. Nakamura, D. Kanekon, S. Yamamoto, K. Maruyama, H. Katsui, T. Goto, High-Temperature Compressive Properties of TiC-Added Mo-Si-B Alloys, JOM. 66 (2014) 1930–1938. https://doi.org/10.1007/s11837-014-1097-6.